A measurement of CMB cluster lensing with SPT and DES year 1 data

E. J. Baxter,[1]⋆ S. Raghunathan,[2] T. M. Crawford,[3,4] P. Fosalba,[5] Z. Hou,[3,4]
G. P. Holder,[6,7,8] Y. Omori,[9] S. Patil,[2] E. Rozo,[10] T. M. C. Abbott,[11] J. Annis,[12]
K. Aylor,[13] A. Benoit-Lévy,[14,15,16] B. A. Benson,[3,4,12] E. Bertin,[14,16] L. Bleem,[3,17,18]
E. Buckley-Geer,[12] D. L. Burke,[19,20] J. Carlstrom,[3,4,17,18,21] A. Carnero Rosell,[22,23]
M. Carrasco Kind,[7,24] J. Carretero,[25] C. L. Chang,[3,4,18] H.-M. Cho,[20]
A. T. Crites,[4,26] M. Crocce,[5] C. E. Cunha,[19] L. N. da Costa,[22,23] C. B. D'Andrea,[1]
C. Davis,[19] T. de Haan,[9,27] S. Desai,[28] J. P. Dietrich,[29,30] M. A. Dobbs,[6,9]
S. Dodelson,[3,12] P. Doel,[15] A. Drlica-Wagner,[12] J. Estrada,[12] W. B. Everett,[31]
A. Fausti Neto,[22] B. Flaugher,[12] J. Frieman,[3,12] J. García-Bellido,[32] E. M. George,[27,33]
E. Gaztanaga,[5] T. Giannantonio,[34,35,36] D. Gruen,[19,20] R. A. Gruendl,[7,24]
J. Gschwend,[22,23] G. Gutierrez,[12] N. W. Halverson,[31,37] N. L. Harrington,[27]
W. G. Hartley,[15,38] W. L. Holzapfel,[27] K. Honscheid,[39,40] J. D. Hrubes,[41] B. Jain,[1]
D. J. James,[42] M. Jarvis,[1] T. Jeltema,[43] L. Knox,[13] E. Krause,[19] K. Kuehn,[44]
S. Kuhlmann,[18] N. Kuropatkin,[12] O. Lahav,[15] A. T. Lee,[27,45] E. M. Leitch,[3,4]
T. S. Li,[12] M. Lima,[22,46] D. Luong-Van,[41] A. Manzotti,[3,4] M. March,[1]
D. P. Marrone,[47] J. L. Marshall,[48] P. Martini,[39,49] J. J. McMahon,[50] P. Melchior,[51]
F. Menanteau,[7,24] S. S. Meyer,[3,4,21,26] C. J. Miller,[52,50] R. Miquel,[25,53]
L. M. Mocanu,[3,4] J. J. Mohr,[29,30,54] T. Natoli,[55] B. Nord,[12] R. L. C. Ogando,[22,23]
S. Padin,[3,4] A. A. Plazas,[56] C. Pryke,[57] D. Rapetti,[58,59]† C. L. Reichardt,[2]
A. K. Romer,[60] A. Roodman,[19,20] J. E. Ruhl,[61] E. Rykoff,[19,20] M. Sako,[1] E. Sanchez,[62]
J. T. Sayre,[31,61] V. Scarpine,[12] K. K. Schaffer,[3,21,26] R. Schindler,[20] M. Schubnell,[50]
I. Sevilla-Noarbe,[62] E. Shirokoff,[3,4,27] M. Smith,[63] R. C. Smith,[11] M. Soares-Santos,[12]
F. Sobreira,[22,64] Z. Staniszewski,[61,65] A. Stark,[66] K. Story,[3,17,19,67] E. Suchyta,[68]
G. Tarle,[50] D. Thomas,[69] M. A. Troxel,[39,40] K. Vanderlinde,[55,70] J. D. Vieira,[7,8]
A. R. Walker,[11] R. Williamson,[3,4] Y. Zhang[12] and J. Zuntz[71]

Affiliations are listed at the end of the paper

ABSTRACT

Clusters of galaxies gravitationally lens the cosmic microwave background (CMB) radiation, resulting in a distinct imprint in the CMB on arcminute scales. Measurement of this effect offers a promising way to constrain the masses of galaxy clusters, particularly those at high redshift. We use CMB maps from the South Pole Telescope Sunyaev–Zel'dovich (SZ) survey

⋆ E-Mail: ebax@sas.upenn.edu
† NASA Postdoctoral Program Senior Fellow.

to measure the CMB lensing signal around galaxy clusters identified in optical imaging from first year observations of the Dark Energy Survey. The cluster catalogue used in this analysis contains 3697 members with mean redshift of $\bar{z} = 0.45$. We detect lensing of the CMB by the galaxy clusters at 8.1σ significance. Using the measured lensing signal, we constrain the amplitude of the relation between cluster mass and optical richness to roughly 17 per cent precision, finding good agreement with recent constraints obtained with galaxy lensing. The error budget is dominated by statistical noise but includes significant contributions from systematic biases due to the thermal SZ effect and cluster miscentring.

1 INTRODUCTION

Cosmic microwave background (CMB) photons passing near massive galaxy clusters are gravitationally deflected, leading to small-amplitude (typically $\lesssim 10\,\mu K$) distortions in the observed CMB on arcminute scales. As pointed out by several authors (e.g. Seljak & Zaldarriaga 2000; Dodelson 2004; Holder & Kosowsky 2004; Vale, Amblard & White 2004; Lewis & King 2006; Hu, DeDeo & Vale 2007), these distortions can be used to measure the masses of galaxy clusters. Because gravitational lensing is sensitive to the total cluster mass, cluster masses determined from the CMB lensing signal are in principle robust to uncertainties on baryonic processes occurring inside the clusters. In contrast, cluster observables such as the thermal Sunyaev–Zel'dovich (tSZ) decrement, X-ray temperature, and cluster richness may depend on complicated baryonic physics that can introduce systematic uncertainty into the cluster mass-observable relations. Systematic uncertainty on cluster masses dominates the error budget of most recent cluster abundance constraints on cosmology (e.g. Rozo et al. 2010; Mantz et al. 2015; de Haan et al. 2016; Planck Collaboration XXIV 2016).

Cluster masses can also be inferred from gravitationally induced shearing of images of background galaxies (for a review see Hoekstra et al. 2013). However, at high redshift, measurements of cluster masses with galaxy lensing become challenging because the source galaxies become harder to detect and their shapes and redshifts become more difficult to measure (e.g. Hoekstra 2001). CMB cluster lensing, on the other hand, has the advantage that the signal to noise is roughly constant with cluster redshift (Lewis & King 2006). Furthermore, CMB cluster lensing is not sensitive to many of the sources of systematic error that affect estimates of cluster mass derived from galaxy shear, including PSF modelling errors (e.g. Jarvis et al. 2016), biases in the photometric redshift estimates of source galaxies (e.g. Melchior et al. 2017), and contamination of the shear sample with unlensed cluster galaxies (e.g. Applegate et al. 2014; Melchior et al. 2017). Consequently, even at low redshifts where CMB lensing-derived constraints on cluster masses may not be statistically competitive with galaxy lensing-derived constraints, CMB cluster lensing offers an important test of systematic errors associated with galaxy lensing.

The CMB lensing signal induced by galaxy clusters was first measured around clusters detected in the South Pole Telescope (SPT) SZ Survey by Baxter et al. (2015, hereafter B15). A similar measurement around *Planck*-detected clusters was performed in Planck Collaboration XXIV (2016). Both of these early measurements used the CMB cluster lensing signal to place (weak) constraints on the scaling between the lensing-derived mass and the mass inferred from measurement of the tSZ. Related work by Madhavacheril et al. (2015) used CMB lensing to constrain the mean mass of optically selected CMASS galaxies (Eisenstein et al. 2011;

Dawson et al. 2013; Ahn et al. 2014) using CMB data from the Atacama Cosmology Telescope Polarimeter (ACTPol). Recently, Geach & Peacock (2017) used CMB lensing measurements derived from *Planck* data to constrain the masses of clusters detected in the Sloan Digital Sky Survey.

The aim of this work is to measure the CMB cluster lensing signal around galaxy clusters identified in optical imaging from year 1 (Y1) Dark Energy Survey (DES) observations and to use the measurement of CMB cluster lensing to calibrate the relation between cluster mass and optical richness. To this end, we employ the same SPT-SZ CMB temperature maps as used in B15. However, the galaxy cluster sample employed here is significantly expanded relative to that used in B15. B15 measured the CMB cluster lensing signal using 513 SZ-selected clusters; here we use 3697 clusters identified using the redMaPPer (Rykoff et al. 2014) algorithm applied to DES imaging.

This work also represents a significant departure in methodology from the B15 analysis. B15 defined a map-space likelihood for the observed CMB temperature measurements around a cluster as a function of cluster mass, and used that likelihood to constrain the stacked cluster mass of the sample. In this work, we employ the more standard quadratic estimator approach to estimate the lensing convergence, κ, in small cutouts of the CMB around the galaxy clusters. The primary advantage of the quadratic estimator approach employed here is its robustness to important sources of systematic error. With minor modification to the standard filters used to construct the quadratic estimator, we find that the estimator is fairly robust to the presence of tSZ signal around the cluster. Additionally, the quadratic estimator is less sensitive to other sources of systematic error, such as foreground lensing. Consequently, in this analysis we are able to directly use the low-noise 150 GHz CMB maps from the SPT rather than creating higher noise tSZ-free maps from multifrequency data.

We fit the stacked CMB lensing-derived κ measurements around the redMaPPer clusters to place constraints on the redMaPPer mass–richness relation. We show that two important sources of systematic error for these constraints are cluster miscentring and contamination of the lensing estimator by tSZ signal.

The structure of the paper is as follows: in Section 2 we introduce the formalism for computing κ from CMB temperature maps around clusters; Section 3 describes the SPT and DES data sets used in this work; Section 4 describes the pipeline we have developed for measuring CMB lensing around galaxy clusters; Section 5 describes the process of fitting the lensing measurements to obtain constraints on the masses of the clusters in our sample; Section 6 describes the simulations we have developed to test the analysis pipeline. Our results are described in Section 7 and discussion of these results is presented in Section 8.

Throughout this analysis we assume the best-fitting ΛCDM cosmological model from the *Planck* TT,TE,EE+lowP fits in Planck Collaboration XIII (2016). Cluster masses are described in terms of M_{200m}, the mass enclosed within a sphere of radius R_{200m} centred on the cluster. R_{200m} is in turn the distance from the cluster centre at which the mean enclosed density is 200 times the mean density of the Universe at the redshift of the cluster.

2 A QUADRATIC ESTIMATOR FOR κ

Gravitational lensing of the CMB remaps the image of the last scattering surface. The observed temperature in direction $\hat{n}$ is equal to the unlensed temperature shifted by the deflection angle, $\nabla\phi$:

$$T(\hat{n}) = \bar{T}(\hat{n} + \nabla\phi), \tag{1}$$

where the overbar is used to indicate unlensed quantities, and ϕ is the lensing potential. The lensing potential is in turn related to the convergence, κ, via

$$\kappa = -\frac{1}{2}\nabla^2\phi. \tag{2}$$

As a result of diffusion damping, the primordial CMB has little power on arcminute scales. Because the deflections induced by cluster lensing are at most a few arcminutes we can approximate the CMB as a pure gradient over the scales at which the deflections are occurring. This allows us to re-write the temperature of the lensed CMB as

$$T \approx \bar{T} + \nabla\bar{T} \cdot \nabla\phi, \tag{3}$$

where we have suppressed the dependence on $\hat{n}$ for clarity. equation (3) makes it apparent that lensing introduces a correlation between fluctuations in CMB temperature field and the background gradient field. The quadratic estimator introduced by Hu & Okamoto (2002) recovers an estimate of κ by identifying these correlations in the maps: a filtered gradient map is multiplied by a high-pass filtered temperature map (see below). This estimator is quadratic in the sense that it involves two powers of the temperature field. Hu & Okamoto (2002) showed how to construct Fourier-space filters that give the minimum variance estimate of κ in this approach.

As pointed out by Hu et al. (2007) and others, the quadratic estimator formulated by Hu & Okamoto (2002) is biased in regions of high κ. This bias can be understood as resulting from the fact that a very massive lens (such as a cluster) will magnify the CMB gradient behind it, effectively decreasing the magnitude of the estimated gradient field; the result is that the κ estimate is biased low. To remove this bias, Hu et al. (2007) showed that one could simply apply an additional low-pass filter to the maps before estimating the gradient field. This additional filter separates out the scales used to estimate the gradient from those used to measure the small-scale CMB fluctuations caused by lensing, and thereby removes the bias. The filter scale used, l_G, becomes an additional parameter of the analysis, but the results are not expected to be very sensitive to variations in this scale.

Explicitly, the Hu et al. (2007) estimator for κ is

$$\frac{\hat{\kappa}_l}{A_l} = -\int d^2\hat{n}\, e^{-i\hat{n}\cdot l}\text{Re}\left\{\nabla\cdot[G(\hat{n})L(\hat{n})]\right\}, \tag{4}$$

where $G(\hat{n})$ is the filtered gradient field, $L(\hat{n})$ is the filtered temperature field, and A_l is a normalization term. The filtered gradient field can be written in Fourier space as

$$G(l) = il W_l T_l, \tag{5}$$

where T_l is the Fourier transform of the temperature field and W_l represents the filter function. Following Hu et al. (2007), we set

$$W_l = \begin{cases} \bar{C}_l\,(C_l + N_l)^{-1} & \text{if} \quad l \leq l_G \\ 0 & \text{if} \quad l > l_G, \end{cases} \tag{6}$$

where C_l ($\bar{C}_l$) is the (un)lensed temperature power spectrum, $N(l)$ is the noise power spectrum, and l_G is the parameter that controls the gradient filter scale. The filtered temperature map is generated using inverse variance weighting:

$$L(l) = \overline{W}_l T_l, \tag{7}$$

with $\overline{W}_l = (C_l + N_l)^{-1}$.

In order to return an unbiased estimate of κ, the normalization factor A_l introduced in equation (4) should be

$$\frac{1}{A_l} = \frac{2}{l^2}\int\frac{dl_1}{(2\pi)^2} l\cdot l_1 W_{l_1}\overline{W}_{l_2} f^{TT}(l_1, l_2), \tag{8}$$

where

$$f^{TT}(l_1, l_2) = (l\cdot l_1)\bar{C}_{l_1} + (l\cdot l_2)\bar{C}_{l_2}, \tag{9}$$

and $l = l_1 + l_2$.

In the analysis presented below, we will apply the Hu et al. (2007) quadratic estimator to estimate κ in cutouts of the SPT CMB maps around galaxy clusters. Because κ is directly related to the integrated mass along the line of sight, by fitting a model to the recovered κ we can extract constraints on the masses of the clusters in our sample.

3 DATA

3.1 CMB maps from SPT

The SPT is a 10-metre millimetre/submillimetre telescope operating at the geographical South Pole (Carlstrom et al. 2011). The CMB maps used in this analysis are from the 2500 deg² SPT-SZ survey, which mapped the sky in three frequency bands centred at 95, 150, and 220 GHz over an observation period from 2008 to 2011 (Story et al. 2013). We use only the SPT 150 GHz maps in this analysis as these have the lowest noise.

SPT observations are divided into patches of the sky (*fields*) that each have an area $\gtrsim 100$ deg². For most fields, SPT scans the sky in strips of constant elevation, first moving left, then right, followed by a step in elevation. For one field (ra21hdec-50), a modified scanning strategy was used for some observations, but we use only the azimuthal scan data from that field in this analysis. The time ordered data from these scans is filtered to prevent aliasing of high-frequency noise and to remove atmospheric and instrumental noise. The time ordered data is processed into maps with 0.5 arcmin resolution using the Lambert equal-area azimuthal projection. The maps used here are identical to those used in the George et al. (2015, hereafter G15) analysis, and we refer readers to that work for more details of the map making process.

The signal on the sky observed with the SPT is modified by a response function consisting of a beam function and a transfer function. The beam function describes the smearing of sky sources as a result of the finite aperture of the SPT primary mirror. The transfer function accounts for time-domain filtering applied to the SPT signal. The total SPT response function to a mode l on the sky can be modelled as the product $B(l)T(l)$, where $B(l)$ and $T(l)$ are the beam and transfer functions, respectively, and $B(l)$ only depends on $l = |l|$ since the beam is close to rotationally invariant.

The amount of time spent observing each field in the SPT-SZ survey is not constant, and the effective depth across a field varies

slightly as a result of scanning strategy. To characterize the varying depth levels between fields and within a field, we define the weight, ω_i, at map pixel i. The weight is roughly proportional to the inverse variance of the map noise at that pixel. We will use maps of the weight across the sky to calculate the appropriate noise power spectrum for each cluster cutout.

Before computing κ from the CMB maps, point sources detected in the maps at 5σ are masked and inpainted with Gaussian noise that matches the noise level of the SPT maps. The point source catalogue used for this purpose is the same as used in George et al. (2015) for masking.

3.2 redMaPPer cluster catalogue from DES

DES is a five-year optical imaging survey of 5000 deg^2 of the southern sky using the Dark Energy Camera on the Blanco Telescope (Flaugher et al. 2015). In this analysis, we make use of first year (Y1) DES data, which covers roughly 1800 deg^2 of sky (Diehl et al. 2014; Drlica-Wagner et al. 2017). The total area of overlap between Y1 observations and the SPT-SZ survey is roughly 1500 deg^2.

Galaxy clusters were identified in the Y1 data using the redMaPPer algorithm (Rykoff et al. 2014). The application of redMaPPer to early DES Science Verification (SV) data is described in Rykoff et al. (2016). The application of redMaPPer to Y1 data will be described in more detail in an upcoming publication (McClintock et al. in preparation). redMaPPer identifies cluster candidates as overdensities of red-sequence galaxies on the sky. For each cluster candidate, redMaPPer determines a list of possible cluster member galaxies and their corresponding membership probabilities. The redMaPPer estimate of the cluster richness, λ, is defined as the sum over these membership probabilities for each cluster. redMaPPer also computes centring probabilities, $P_{\rm cen}$, which characterize the probability that a member galaxy is at the centre of the cluster. We treat the galaxy with the highest $P_{\rm cen}$ as the cluster centre in this analysis, but also consider the effects of various degrees of miscentring. We will also use the redMaPPer estimates of the cluster redshifts in this analysis; these are expected to be accurate to roughly $\sigma_z \sim 0.01(1 + z)$.

We consider only the volume-limited redMaPPer DES Y1 catalogue, restricted to clusters with richness $\lambda > 20$, resulting in a total of 7066 clusters. We further impose the requirements that the minimum SPT-defined weight in a $\sim 2° \times 2°$ cutout around the cluster (see Section 4 for a more detailed description of the cutouts) is greater than zero and is at least 80 per cent of the weight at the cluster location. These restrictions ensure that we do not include clusters outside of the SPT fields or clusters for which the weight is varying significantly across the cutout (as may occur near the field boundaries). After imposing this restriction, the cluster catalogue is reduced to 4552 clusters. Finally, as will be described in more detail in Section 7.3.1, we find that the presence of tSZ signal around high-mass clusters can bias the κ reconstruction. Because the amplitude of the tSZ signal scales as $M^{5/3}$, by restricting our analysis to lower mass clusters we find that we can reduce the tSZ bias to acceptable levels while preserving much of the lensing signal. To this end, we employ a somewhat conservative richness cut, restricting our analysis to $\lambda < 40$. This richness threshold corresponds to a mass of about 3.2×10^{14} M$_\odot$ assuming the mass–richness relation of Melchior et al. (2017, hereafter M17). We discuss the motivation for the richness cut and tests of potential tSZ biases in more detail in Section 7.3. Imposing the richness cut yields a final catalogue of 3697 clusters ranging in redshift from roughly $z \sim 0.1$ to 0.7, with mean redshift $\bar{z} = 0.45$.

4 MEASUREMENT OF κ

For each DES-identified cluster, we estimate κ using cluster-centred cutouts from the SPT 150 GHz temperature maps presented in G15. The CMB temperature maps are pixelized at 0.5 arcmin resolution and the cutouts are 256 pixels on a side.

We rotate each cutout so that it is aligned along lines of constant azimuth and elevation (see e.g. Schaffer et al. 2011 for description of the rotation angles corresponding to the Lambert equal-area azimuthal projection). Aligning the cutouts with altitude and azimuth ensures that the transfer function is the same for every cutout, significantly simplifying the subsequent analysis. Rotation is performed using third-order spline interpolation. The rotated cutouts are then apodized using a Tukey window with $\alpha = 0.1$. Our analysis of simulated data in Section 6 confirms that this choice of apodization is reasonable.

The SPT beam and transfer functions are deconvolved from the cutouts before the application of the quadratic estimator. Estimates of the beam functions used for this purpose are described in Story et al. (2013). The transfer function deconvolved from each cutout is an analytic approximation to the true transfer function consisting of three pieces:

$$T(\boldsymbol{l}) = F_1(\boldsymbol{l})F_2(\boldsymbol{l})F_3(\boldsymbol{l}), \tag{10}$$

where

$$F_1(\boldsymbol{l}) = \exp(-(l_1/l)^6), \tag{11}$$

$$F_2(\boldsymbol{l}) = \exp(-(l_2/l_x)^6), \tag{12}$$

$$F_3(\boldsymbol{l}) = \exp(-(l_x/l_3)^6), \tag{13}$$

with $l_1 = 500$, $l_2 = 400$, and $l_3 = 15\,000$. We have checked that there is negligible difference between the deconvolved cutouts obtained using the above transfer function approximation and the deconvolved cutouts obtained using a more accurate estimate of the transfer function that was computed by mock observing a δ-function signal located at the centre of the field. To prevent highly filtered modes from introducing numerical problems as a result of deconvolution, we additionally filter each cutout to remove modes with $l < l_1$, $l_x < l_2$, and $l_x > l_3$.

4.1 Noise and foregrounds

Estimating κ near each cluster requires an estimate of the noise power spectrum in each CMB temperature cutout. We consider as noise any contribution to the cutouts that is not CMB and that is not expected to be correlated with the positions of the galaxy clusters. Non-CMB signal that is correlated with the clusters – such as the cluster tSZ signal – is treated as a source of systematic error and is discussed in Section 7.3. Each cutout receives contributions from astronomical, atmospheric, and instrumental noise sources. We will take a model-based approach to estimating the contributions from astronomical noise sources; we estimate the contribution from atmospheric and instrumental noise directly from the data.

We first consider the contribution to the cutouts from astronomical noise sources; such noise is constant over the time-scale of the observations. In addition to the CMB, the sky signal at 150 GHz receives significant contributions from several sources, including galaxies that are bright at microwave frequencies and unresolved tSZ signal. The relative contributions of these various sources is l-dependent: at low multipoles ($\ell \lesssim 3000$), the CMB dominates

while at higher multipoles ($\ell \gtrsim 3000$), foreground emission becomes dominant. In general, the astrophysical foreground sources can be approximated as Gaussian random noise. Although foreground emission from extragalactic sources such as dusty galaxies and the tSZ are known to be non-Gaussian at some level (e.g. Crawford et al. 2014), the Gaussian approximation should be sufficient for the noise levels considered here (van Engelen et al. 2014). The SPT CMB maps also receive some contribution from galactic foregrounds, such as dust. However, this foreground contribution is expected to be significantly below the contributions from the other foregrounds mentioned above (e.g. Keisler et al. 2011).

Once bright point sources have been removed, the dominant foreground contribution to the sky at 150 GHz comes from dusty, star-forming galaxies (DSFGs). The power spectrum of DSFG emission can be divided into two components: one arising from sources on the sky that are unclustered, and another arising from sources that are clustered on the sky. The unclustered component has an angular power spectrum given by $C_l = C_0$, where C_0 is a constant. Expressed in terms of $D_l = l(l+1)C_l/(2\pi)$, the analysis of G15 found $D_{3000} = 9.16 \pm 0.36 \,\mu\text{K}^2$ for the unclustered component. The clustered DSFG component, on the other hand, can be modelled with $D_l \propto l^{0.8}$ for $l > 1500$. The G15 analysis found $D_{3000} = 3.46 \pm 0.54 \,\mu\text{K}^2$ for this component. For $l < 1500$, the contribution of the clustered DSFG foreground can be ignored.

Two other significant foreground contributors at 150 GHz are radio galaxy emission below the detection threshold of SPT maps and the tSZ signal from undetected galaxy groups or clusters. Following G15, we model the signal from radio galaxies below the SPT detection threshold as an unclustered component with $D_{3000} = 1.28 \,\mu\text{K}^2$. To model the tSZ signal from sources below the detection threshold we use the templates from Shaw et al. (2010), normalized using the constraint from G15. G15 constrained the amplitude of the tSZ power spectrum after masking sources above the detection threshold to be $D_{3000} = 2.33^{+0.8}_{-1.4} \,\mu\text{K}^2$, and we use this value here.

For our fiducial analysis we make the simplifying approximation that all emission from astrophysical foregrounds is unlensed by the galaxy clusters. In reality, this approximation is not very good. The cosmic infrared background (CIB), for instance, is expected to receive significant contribution from redshifts $1 < z < 3$ (e.g. Béthermin et al. 2013). Because the clusters used in this analysis have $\bar{z} = 0.45$, a significant portion of the CIB may be lensed by the clusters. However, the precise redshift distribution of the DSFGs and other foreground sources is not known, making modelling of foreground lensing difficult. While treating the foregrounds as unlensed is incorrect at some level, we will show in Section 7.3.2 that this simplifying assumption has little effect on our results.

Unlike astrophysical foregrounds, the contribution from atmospheric and instrumental noise sources is not constant over the SPT observation time, allowing us to estimate the contributions to the noise power spectrum from these sources by differencing maps constructed from observations taken at different times. As described in Section 3.1, SPT fields are observed by scanning the telescope left and right across the full field at a series of discrete elevations. We can form a signal-free map as the combination $\boldsymbol{m}^{\text{diff}} = (\boldsymbol{m}_{\text{L}} - \boldsymbol{m}_{\text{R}})/2$, where $\boldsymbol{m}_{\text{L}}$ and $\boldsymbol{m}_{\text{R}}$ are the maps formed from left and right-going scans, respectively. Because atmospheric and instrumental noise vary on time-scales that are much shorter than the time difference between the $\boldsymbol{m}_{\text{L}}$ and $\boldsymbol{m}_{\text{R}}$ observations, $\boldsymbol{m}^{\text{diff}}$ should provide a realization of the instrumental and atmospheric noise.

The SPT-SZ survey spent different amounts of time observing each field, resulting in field-to-field variations in the effective noise levels of the resultant CMB maps. Additional variation in the noise levels between and within fields occurs as a result of sky projection. To account for field-to-field variation in the noise level, each cluster is analysed using the difference maps for the field in which it was observed. To account for variation in the noise level across the field, we use the SPT weight maps, $\boldsymbol{\omega}$.

We first construct a scaled difference map that has effectively uniform weight by multiplying the map by $\sqrt{\boldsymbol{\omega}/\langle\omega\rangle}$, where $\langle\omega\rangle$ is the mean weight across the inner $[0.3, 0.7]$ of the map. We then compute the instrumental and atmospheric noise power spectrum at the mean weight using this scaled difference map. To determine the estimate of the instrumental and atmospheric noise power spectrum for the ith cutout we then rescale the noise power spectrum estimate for the scaled difference map by $\langle\omega\rangle/\omega_i$, where ω_i is the mean weight across the ith cutout.

Finally, because we deconvolve the beam and transfer functions from the cutouts before applying the quadratic estimator, we must account for this in the noise power spectrum estimate. The total noise power spectrum estimate for the ith cutout is then

$$N_i(\boldsymbol{l}) = N_F(\boldsymbol{l}) + \frac{\langle\omega\rangle}{\omega_i} \frac{N_{\text{IA}}(\boldsymbol{l})}{[B(\boldsymbol{l})T(\boldsymbol{l})]^2}, \qquad (14)$$

where $N_F(\boldsymbol{l})$ is the estimate of the noise contribution from the astrophysical foregrounds described above, N_{IA} is the estimate of the instrumental and atmospheric noise from the scaled difference map, and $B(\boldsymbol{l})$ and $T(\boldsymbol{l})$ are the beam and transfer function estimates, respectively. The estimate of the foreground noise contribution has no beam or transfer function by construction, so it does not require the beam or transfer function to be deconvolved.

4.2 Stacked, filtered κ estimate

Given the beam and transfer function deconvolved cutouts and the estimate of the noise power spectrum in the cutout, we compute κ across the cutouts as described in Section 2. When generating the κ estimate for each cutout we use a gradient filter scale of $l_G = 1500$. In principle, higher signal to noise could be achieved by setting $l_G = 2000$ as originally suggested by Hu et al. (2007). However, we have found in tests on simulated data (see Section 7.3.1) that the tSZ signal from massive clusters can lead to a significant bias in the recovered mass when using $l_G = 2000$. By using the lower value of $l_G = 1500$, we find that this bias can be significantly reduced without significantly degrading the signal to noise. The low-pass filter removes some of the highly localized tSZ signal while preserving most of the information about the large-scale gradient in the CMB near the cluster.

By deconvolving the beam function from the cutouts, we increase the effective noise of small-scale modes that are heavily filtered by the beam [e.g. equation (14)]. Such small-scale noise is problematic for our analysis since we attempt to fit the κ profiles of the clusters in real space. In real space the filtered scales are not cleanly separated from the unfiltered scales, and the resultant small-scale noise introduces numerical problems. To reduce the effects of such noise, we filter the κ cutouts with a low-pass filter to remove modes with $l < \sqrt{8\ln 2}/\theta_{\text{FWHM}}$, where $\theta_{\text{FWHM}} = 1.3$ arcmin is chosen to roughly match the beam size of the SPT.

Because the estimate of κ at the cluster location depends on the gradient of the CMB temperature field, there is useful information for constraining κ in the temperature maps at scales well beyond the halo virial radius. However, once the estimate of κ has been

computed, areas of the κ cutout that are well beyond the virial radius of the cluster do not contain significant information about the halo density profile.[1] We can therefore speed up our analysis pipeline with little reduction in signal to noise by restricting our analysis to the inner parts of the κ cutouts. To this end, we restrict our fitting to the inner 10 arcmin $\times$ 10 arcmin region at the centre of the full κ cutouts. The size of this reduced cutout can be compared to the halo virial radius of a $M = 5 \times 10^{14}\,\mathrm{M}_\odot$ halo at the mean redshift of the cluster sample ($\bar{z} = 0.45$), which is $\sim$5 arcmin. As noted previously, the richness limit imposed in this analysis corresponds to roughly $3.25 \times 10^{14}\,\mathrm{M}_\odot$, so restricting the analysis to the inner 10 arcmin captures the region within the virial radius for the majority (if not all) of the clusters in our sample. To reiterate: we use large 128 arcmin $\times$ 128 arcmin cutouts of the CMB temperature maps to estimate κ, but we only use the inner 10 arcmin $\times$ 10 arcmin of the resulting κ map for cluster mass estimation.

Even if the true κ in the cutout is zero, the application of the quadratic estimator to the cutout is still expected to return a non-zero estimate of κ because of the apodization window that is applied. To estimate the true κ, then, we must subtract an estimate of the mean κ in the absence of any CMB lensing, i.e. the *mean field*. We form an estimate of the mean field for each observation field by performing the κ estimation process around random locations within the field. The number of random points is approximately 40 times the number of clusters in each field, and we confirm that the scatter in the mean field estimate for each field is negligible compared to the noise in the κ estimate around the clusters.

Because the signal to noise for the κ measurements around an individual cluster is much less than 1, we form a stack of the κ cutouts. To maximize the signal to noise of the stack, we use inverse variance weighting when stacking. The stacked κ measurement, $\boldsymbol{\kappa}_s$, is then

$$\boldsymbol{\kappa}_s = \frac{\sum_i w_i \boldsymbol{\kappa}_i}{\sum_i w_i}, \qquad (15)$$

where the sum runs over all cutouts and $w_i = 1/\sigma_i^2$ is the inverse variance weight. The estimate of the variance, σ_i^2, used for weighting is the same for each field and is calculated by taking the variance across all κ cutouts in that field. Note that we do not attempt to perfectly align cluster centres when performing the stacking; instead, we keep track of the full coordinate information for each cutout, and take this into account when constructing the model for the stacked κ cutout. The vector notation for $\boldsymbol{\kappa}_s$ indicates that the measurements are a function of pixel location across the cutout (defined relative to the cluster centre).

Because the SPT transfer function is anisotropic, the κ cutouts necessarily have anisotropic noise. We therefore fit the stacked 2D $\boldsymbol{\kappa}_s$ cutout in our analysis rather than the azimuthally averaged profile of this cutout, as will be described in more detail below. To estimate the covariance of $\boldsymbol{\kappa}_s$ we use jackknifing.

5 FITTING THE κ MEASUREMENTS

5.1 Model

We fit the 2D stacked $\boldsymbol{\kappa}_s$ measurement to constrain the relation between M_{200m} and λ for the clusters in our sample. Each cluster

is modelled as the sum of a '1-halo' term resulting from the mass of the cluster itself, and a '2-halo' term resulting from correlated structure along the line of sight.

We model the 1-halo term of each cluster using the Navarro, Frenk, and White (NFW) (Navarro, Frenk & White 1996) density profile:

$$\rho(x) = \frac{200\rho_m(z)}{3} \left[\frac{c^3(1+c)}{(1+c)\ln(1+c) - c} \right] \frac{1}{x(1+x)^2}, \qquad (16)$$

where $x = rc/R_{200m}$, c is the concentration parameter, and z is the redshift of the cluster. We set c using the mass–concentration relation from Diemer & Kravtsov (2015), but find that our results are essentially unchanged if the mass–concentration relation from Duffy et al. (2008) is used instead. The projected density along the line of sight is then

$$\Sigma_{1h}(R) = \int_{-\infty}^{\infty} dh\, \rho \left(r = \sqrt{R^2 + h^2} \right). \qquad (17)$$

Analytic formulae for Σ_{1h} corresponding to the density profile of equation (16) can be found in e.g. Bartelmann (1996).

We model the 2-halo term following Oguri & Hamana (2011). The projected density profile due to correlated structure along the line of sight is written as

$$\Sigma_{2h}\left(\theta = \frac{R}{D_A(z)} \right) = \int \frac{\ell d\ell}{2\pi} J_0(\ell\theta) \frac{\rho_m(z)b(M)}{(1+z)^3 D_A^2(z)}$$
$$\times P_m\left(k = \frac{\ell}{(1+z)D_A(z)}, z \right), \qquad (18)$$

where $D_A(z)$ is the angular diameter distance to the cluster, J_0 is the zeroth order Bessel function of the first kind, $\rho_m(z)$ is the mean matter density of the Universe, $P_m(k, z)$ is the linear matter power spectrum, and $b(M)$ is the clustering bias of haloes with mass M. We model the halo bias using the fitting formulae from Tinker et al. (2010). The total projected density along the line of sight is then $\Sigma(R) = \Sigma_{1h}(R) + \Sigma_{2h}(R)$.

The lensing convergence, κ, is related to the projected density along the line of sight via $\kappa = \Sigma/\Sigma_c$, where Σ_c is the critical surface density,

$$\Sigma_c = \frac{c^2}{4\pi G} \frac{D_S}{D_L D_{LS}}, \qquad (19)$$

and D_S, D_L, and D_{LS} are the angular diameter distances to the source (i.e. the last scattering surface), the lens (i.e. the cluster), and between the lens and source.

Because our analysis uses cluster centres determined by redMaPPer, we must also account for differences between the redMaPPer-identified centre and the true halo centre, i.e. miscentring. We follow an approach to accounting for miscentring similar to that of M17. A cluster that is miscentred by R_{mis} will result in a projected density profile given by

$$\Sigma_{mis}(R|R_{mis}) = \int_0^{2\pi} \frac{d\theta}{2\pi} \Sigma \left(\sqrt{R^2 + R_{mis}^2 + 2RR_{mis}\cos\theta} \right) \quad (20)$$

where $\Sigma(R)$ is the projected density profile without miscentring (e.g. Yang et al. 2006).

By comparing redMaPPer centres identified in DES SV data measurements in X-ray and SZ, Rykoff et al. (2016) constrained the fraction of miscentred clusters in DES SV data to be $f_{mis} = 0.22 \pm 0.11$. Rykoff et al. (2016) modelled the assumed cluster centre as being a draw from a two-dimensional Gaussian with variance σ_R^2 centred on the true cluster centre. In this model, R_{mis} follows a Rayleigh

---

[1] Large scales do contain information about the halo–matter correlation, which in turn is related to the halo mass. However, our focus here is on measuring the halo mass directly in the '1-halo regime'.

distribution which peaks at σ_R. Rykoff et al. (2016) further assumed that σ_R was proportional to the redMaPPer defined cluster radius, $R_\lambda = (\lambda/100)^{0.2} \, h^{-1}$ Mpc, and constrained $\sigma_R = c_{\rm mis} R_\lambda$ with $\ln c_{\rm mis} = -1.13 \pm 0.22$.

In this analysis, we simply assume that a fraction $f_{\rm mis}$ of the clusters are miscentred by a distance $\sigma_R = c_{\rm mis} R_\lambda$. The miscentred κ profile can then be written as

$$\kappa(R; M_{200m}, z) = \frac{(1 - f_{\rm mis})\Sigma_0(R) + f_{\rm mis}\Sigma_{\rm mis}(R)}{\Sigma_{\rm c}}, \qquad (21)$$

where Σ_0 is the projected NFW density profile without miscentring. In our fiducial analysis, we take the approach of fixing $f_{\rm mis} = 0.22$ and $\ln c_{\rm mis} = -1.13$, i.e. the best-fitting values from M17. We will quantify the uncertainty on our mass–richness constraints that is associated with the miscentring model in Section 7.3.3. The final κ model for a cutout is obtained by convolving the miscentred κ map with the filter described in Section 4.2.

Following several previous studies constraining the mass–richness relation of redMaPPer clusters (e.g. Baxter et al. 2016; M17; Simet et al. 2017), we adopt a power-law relation for the expectation value of the mass, M, at fixed richness and redshift:

$$\langle M | \lambda_i, z_i; \boldsymbol{p}_{\rm m.r.} \rangle = A \left(\frac{\lambda}{\lambda_0} \right)^\alpha \left(\frac{1+z}{1+z_0} \right)^\beta, \qquad (22)$$

where we fix the pivot points at $\lambda_0 = 30$ and $z_0 = 0.5$ to match M17. The parameters of the mass–richness relation are the amplitude, A, the richness scaling, α, and the redshift scaling, β; we denote the vector of these parameters with $\boldsymbol{p}_{\rm m.r.}$.

Given $\boldsymbol{p}_{\rm m.r.}$, our model for the stacked κ profile, κ_s^m, is then the weighted average across all clusters of κ evaluated at the expectation value of the mass for each cluster:

$$\kappa_s^m(\boldsymbol{p}_{\rm m.r.}) = \frac{\sum_i w_i \boldsymbol{\kappa}(\langle M | \lambda_i, z_i; \boldsymbol{p}_{\rm m.r.} \rangle, z_i)}{\sum_i w_i}, \qquad (23)$$

where the w_i are the inverse variance weights introduced in Section 4.2 and $\boldsymbol{\kappa}$ is given by the mis-centred model of equation (21) after application of the filter described in Section 4.2. Below, we will fit the stacked cluster profile $\boldsymbol{\kappa}_s$ with the three parameter model defined in this section.

5.2 Likelihood analysis

We now describe the process of fitting the stacked κ cutout to obtain constraints on the mass–richness relation of the redMaPPer clusters. We begin by assuming a Gaussian likelihood for the data vector, $\boldsymbol{\kappa}_s$, given the model κ_s^m from equation (23):

$$\ln \mathcal{L}(\boldsymbol{\kappa}_s | \boldsymbol{p}_{\rm m.r.}; \{\lambda_i, z_i\}) = -\frac{1}{2} \left[\boldsymbol{\kappa}_s - \boldsymbol{\kappa}_s^m \right]^T \mathbf{C}^{-1} \left[\boldsymbol{\kappa}_s - \boldsymbol{\kappa}_s^m \right], \qquad (24)$$

where $\mathbf{C}$ is the covariance matrix of the $\boldsymbol{\kappa}_s$ measurement estimated using jackknife resampling.

The posterior on the mass–richness parameters can then be written as

$$\mathcal{P}(\boldsymbol{p}_{\rm m.r.} | \boldsymbol{\kappa}_s; \{z_i\}) = \mathcal{L}(\boldsymbol{\kappa}_s | \boldsymbol{p}_{\rm m.r.}; \{\lambda_i, z_i\}) \mathcal{P}(\boldsymbol{p}_{\rm m.r.}), \qquad (25)$$

where the last term, $\mathcal{P}(\boldsymbol{p}_{\rm m.r.})$, represents the priors on the mass–richness parameters. Given the signal to noise of our measurements, we do not expect to be able to robustly constrain many parameters. We therefore focus on constraining the amplitude of the mass–richness relation, A. We impose a flat prior on A between $[10^{12}, 10^{16}]$, but find that our results are quite insensitive to the form of this prior, indicating that our constraints are dominated by information

Table 1. Constraints on the mass–richness parameters. Top-hat distributions are indicated by brackets, while Gaussian distributions are written in the form $a \pm b$.

Parameter	Prior	Posterior
$A/M_\odot$	$[10^{12}, 10^{16}]$	$(2.14 \pm 0.35) \times 10^{14}\,M_\odot$
α	1.23 ± 0.30	1.25 ± 0.30
β	0.18	–

in the likelihood. We impose a Gaussian prior on α motivated by the results of M17 and Simet et al. (2017, hereafter S17). These two analyses found $\alpha = 1.12 \pm 0.20$ and 1.33 ± 0.1, respectively. For the central value of our prior on α, we simply take the average of these two values. For the width of the prior, we assume $\sigma_\alpha = 0.3$. This value is meant to reflect the statistical uncertainty in α along with any uncertainty owing to differences in the definition of richness between M17, S17, and Y1 DES data. As we will show below, our constraint on A is not very degenerate with α, so having a relatively loose prior on α is acceptable. To simplify the analysis, we fix $\beta = 0.18$ (equivalent to assuming a δ-function prior on this parameter), corresponding to the best-fitting value from M17. We find that our analysis is almost entirely insensitive to β, so fixing this parameter has essentially no impact on our results. These priors are summarized in Table 1. The resultant parameter space is two-dimensional (A and α) and can be explored using a simple grid sampler.

Equation (25) ignores several potential sources of uncertainty in the stacked model, κ_s^m. First, we have ignored scatter in the mass–richness relation. This scatter is expected to be described by a lognormal probability distribution function, with scatter at fixed λ given by $\sigma_{\ln M | \lambda} \sim 0.25$ (e.g. Rozo & Rykoff 2014). At low richness, one expects increased scatter due to the Poisson uncertainty in the number of galaxies. However, even accounting for the additional Poisson scatter (following the prescription described in S17) we find that the uncertainty on κ_s^m is much less than the uncertainty on the measurement vector, κ_s. Consequently, without introducing any measurable bias in our results, we can ignore scatter in the mass–richness relation.

Additionally, equation (25) ignores uncertainty in the redshift and richness estimates for the clusters. The typical redshift uncertainty for DES redMaPPer clusters is $\sigma_z/(1 + z) \lesssim 0.01$ (Rykoff et al. 2016). For this level of redshift uncertainty, the resultant uncertainty in κ_s^m is much less than the uncertainty in the κ measurements, so it is safe to ignore redshift uncertainty in this analysis. A similar argument holds for the uncertainty on the richness estimates.

Finally, note that equation (25) ignores correlated scatter between the richness and lensing mass. Such correlated scatter is expected because clusters that are elongated along the line of sight will have enhanced richness and lensing masses. However, the impact of such correlated scatter is expected to be at the few percent level (Melchior et al. 2017), well below the statistical uncertainties obtained here. For simplicity we therefore ignore this effect.

6 PIPELINE VALIDATION

We use simulated SPT observations to test the κ estimation pipeline. We generate simulated SPT maps by adding together Gaussian realizations of the CMB, foreground and noise. The CMB realizations are generated from a power spectrum computed at our fiducial

cosmological model using CAMB[2] (Lewis, Challinor & Lasenby 2000).

We lens the simulated CMB maps with mock clusters described by the NFW profile of equation (16). To perform the lensing operation, we compute the deflection angles for these clusters using the formulae of Bartelmann (1996). The unlensed CMB is then remapped to the lensed CMB with cubic spline interpolation. The main purpose of the simulations is to confirm that our lensing pipeline recovers an unbiased estimate of κ to within our noise levels. We therefore use clusters of fixed mass and redshift when generating the simulations. We use 100 mock galaxy clusters that are roughly equally spaced across the field. Each simulated cluster has $M = 2.5 \times 10^{14}\,\mathrm{M_\odot}$, $z = 0.4$ and $c = 4.8$. This mass is somewhat higher than the mean mass predicted for the redMaPPer sample based on the mass–richness relation of M17, which is $M \sim 2.05 \times 10^{14}\,\mathrm{M_\odot}$.

Foreground emission is generated as Gaussian random realizations of the foreground models described in Section 4.1 and added to the lensed CMB maps. We assume that foreground emission is unlensed by the galaxy clusters when generating the simulated maps because this matches the assumption of our fiducial analysis; we consider the effects of this assumption on the analysis of the real data in Section 7.3.2. Note that for the purposes of pipeline validation, we do not include tSZ signal in the simulated data; we estimate the effects of tSZ contamination in Section 7.3.1.

The simulated sky maps are then convolved with the beam and field-dependent transfer functions from G15. Finally, field-dependent noise realizations are added to the simulated maps. To generate the field-dependent noise realizations, we generate Gaussian random realizations of the estimated noise power spectrum from the weight-scaled difference maps described in Section 4.1. The noise realizations are then scaled by the inverse square root of the weight to account for weight variations across the field.

To build statistics, we generate 200 simulated skies using the methods described above. Each simulated sky map is lensed with 100 clusters, bringing the total number of simulated clusters to 20 000. Each simulated sky has a different random realization of the CMB, foregrounds and noise. The simulated skies are passed through the same pipeline that is applied to the data to extract κ cutouts around each of the simulated clusters. The κ cutouts are then fit to determine constraints on the cluster mass, M_{200m}.

Fig. 1 shows the true, azimuthally averaged κ profile (red) in the simulations compared to the κ profile recovered using our analysis pipeline (points with error bars). The oscillatory behaviour of κ comes from application of the filter described in Section 4.2 to the κ cutouts. The pipeline recovers an unbiased estimate of κ to within the uncertainties of the mock data. Note that we have used roughly five times as many simulated clusters as real clusters for this test to increase our sensitivity to any possible biases in the κ estimation.

7 RESULTS

7.1 κ measurements around redMaPPer clusters

Fig. 2 shows the weighted average of the κ cutouts around redMaPPer clusters, restricted to the region used in fitting. Pixels in the κ cutouts are 0.5 arcmin on a side and the fitted region is
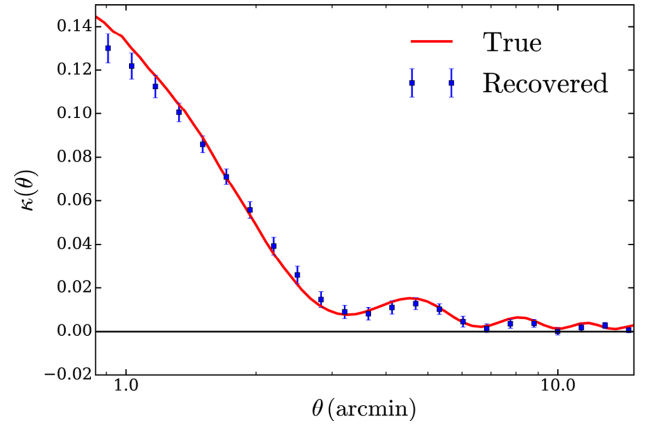

Figure 1. Azimuthally averaged κ profile recovered from analysis of simulated data. Red solid curve shows the true κ profile around mock clusters with $M = 2.5 \times 10^{14}\,\mathrm{M_\odot}$ after the application of the filtering described in Section 4.2. Blue data points with errorbars show recovered κ in the presence of realistic noise, foreground emission, beam, and transfer function using 20 000 clusters. The measurement pipeline recovers an unbiased estimate of the true κ profile to within the uncertainties.
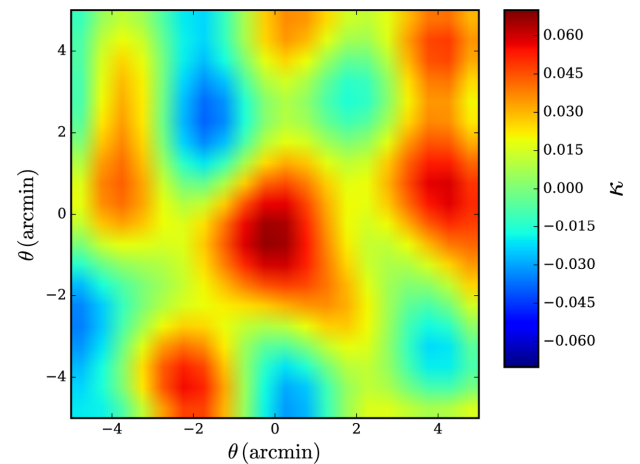

Figure 2. The stacked, weighted 2D κ profile recovered from the analysis of CMB temperature data around 3697 redMaPPer clusters. Each pixel in the cutout is 0.5 arcmin on a side.

20 pixels by 20 pixels. Because the centres of the redMaPPer clusters do not lie at exactly the same position in each map pixel, Fig. 2 incorporates some smearing due to pixelization effects. However, when fitting for the parameters of the mass–richness relation we use the full coordinate information for each pixel relative to the true cluster centres on a cluster-by-cluster basis.[3]

Fig. 3 shows the azimuthally averaged one-dimensional κ profile extracted from the analysis of redMaPPer clusters. To determine the error bars shown in this plot we use a jackknife resampling approach, where the jackknife subsamples are determined by dividing survey area into 100 regions of approximately equal area. The data exhibit

---

[2] http://camb.info

---

[3] A small offset in the peak of the recovered convergence map relative to the origin may be observed in Fig. 2, which we attribute to noise. A similar effect is seen when applying the quadratic estimator to the simulations described in Section 6; such an offset was also observed in Madhavacheril et al. (2015). Averaged over many realizations, though, we correctly recover the input convergence maps in the simulations.
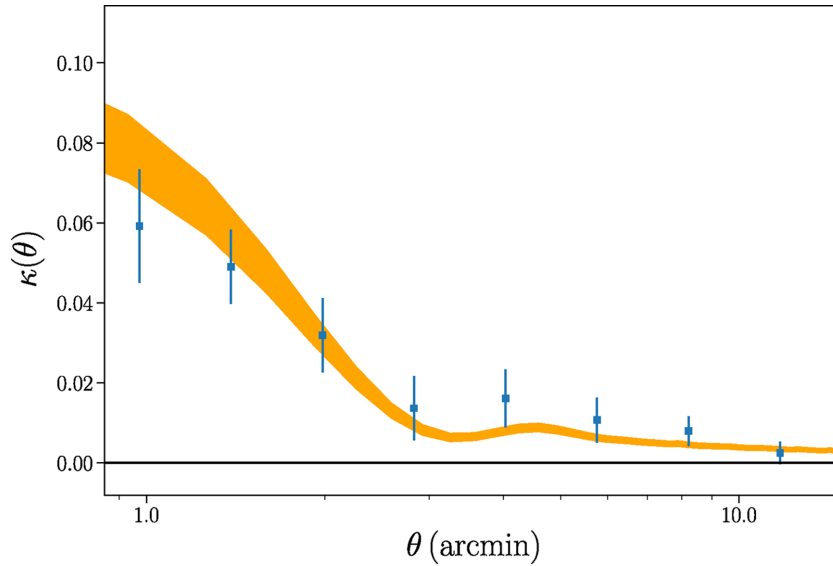
Figure 3. The azimuthally averaged κ profile recovered from measurement of CMB lensing around 3697 redMaPPer clusters detected in DES Y1 data (blue points with errorbars). The errorbars shown are the diagonal elements of the full covariance determined from a jackknife resampling of the cluster sample; there is significant covariance between adjacent data points. The orange region indicates the allowed range of model predictions (68 per cent confidence region) given the results of the fit for parameters of the cluster mass–richness relation.

a strong preference for increasing κ towards the centre of the cluster, as expected. We note, though, that adjacent measurements in Fig. 3 are highly correlated. While we show the 1D κ profile here for the purposes of visualization, our analysis to extract mass constraints on the clusters uses the full 2D κ information, rather than the 1D azimuthally averaged profile.

7.2 Fit results

The 2D and marginalized posteriors on the mass–richness parameters A and α recovered from our analysis are shown in Fig. 4; numerical results are given in Table 1. We find $A/M_\odot = (2.14 \pm 0.35) \times 10^{14}$, a roughly 17 per cent constraint on the amplitude of the mass–richness relation. The posterior on α is entirely dominated by the prior (shown as the blue curve). This is not surprising given the fairly low signal to noise of our measurement and the fact that the richness range of the sample is restricted to $20 < \lambda < 40$. There appears to be minimal degeneracy between A and α over the range of α allowed by the constraints of M17 and S17. If we fix α to the best-fitting value from M17, we find that the best-fitting A changes by only 1 per cent and the error on A decreases by only 2 per cent. Because our prior on α is quite wide, our results are therefore very robust to assumptions about α.

We find $\Delta \ln \mathcal{L} = 33.3$ between the peak of the likelihood and $A = 0$; a likelihood ratio test therefore allows us to reject the null hypothesis that $A = 0$ at 8.1σ significance. The significance of this detection can be compared to the 3.1σ detection obtained in B15 from 513 clusters. Those clusters were approximately twice as massive as the ones considered here, so would expect that despite the increase in sample size our current measurement would yield a $\sim 4.0\sigma$ detection. The higher detection significance reported here is the result of the switch from the tSZ-free maps used in B15 to the lower noise 150 GHz SPT maps that we are able to use with the quadratic estimator in the current analysis.
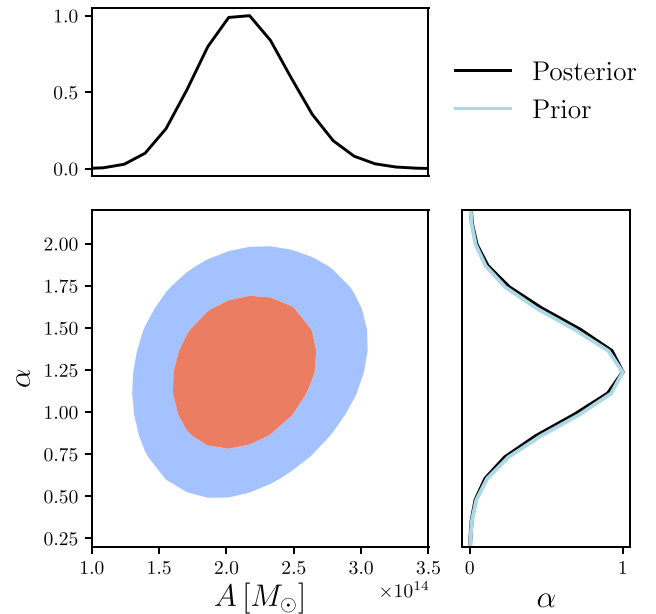
Figure 4. Constraints on the amplitude, A, and richness scaling, α, of the redMaPPer mass–richness relation obtained from fits to CMB lensing measurements. Contours represent 1σ and 2σ levels. The blue curve in the panel at right shows the prior on α, which dominates our constraint. Numerical results are summarized in Table 1.

7.3 Systematic errors

7.3.1 tSZ

The tSZ effect is caused by inverse Compton scattering of CMB photons with energetic electrons. The effect is especially pronounced in the direction of massive galaxy clusters, as these objects are reservoirs of hot gas. At 150 GHz – the frequency of observation for the CMB maps used in this analysis – the tSZ effect leads to a decrement in the observed CMB temperature near the cluster (for a

review see Birkinshaw 1999). We do not attempt to model the tSZ in this analysis; consequently, its presence acts as a potential source of bias to our measurement of κ. Somewhat worryingly, the magnitude of the tSZ decrement for a massive cluster can be $\sim 100\,\mu K$, significantly larger than the magnitude of the CMB cluster lensing-induced distortion, which has amplitudes $\lesssim 10\,\mu K$. However, the situation is not so bad as it might first appear: unlike the CMB cluster lensing signal, the tSZ effect is not correlated with the CMB gradient behind the cluster. Because the quadratic estimator used to measure the lensing distortion is effectively picking out correlations between small-scale CMB distortions and the larger scale gradient field, it is expected to be fairly robust to tSZ contamination. Furthermore, the low-pass filtering imposed on the CMB maps to estimate the gradient field (Section 2) effectively filters out the small-scale tSZ decrements, reducing their contamination of the κ estimator. Finally, as noted in Section 3.2, we restrict our analysis to clusters with $\lambda < 40$ to reduce the amplitude of tSZ contamination.

To constrain the level of systematic error introduced to our κ estimates by the tSZ we rely on simulations. We introduce mock tSZ signals into the simulations described in Section 6 and re-analyse these simulations to determine how much the κ estimation is biased. The mock tSZ signals used for this purpose are taken from the hydrodynamical simulations of Le Brun et al. (2014). These simulations represent an extension of the OverWhelmingly Large Simulations project (Schaye et al. 2010), and are designed with applications to cluster cosmology in mind. To this end, the simulations are large volume (400 h^{-1} Mpc on a side) and include computation of maps of the Compton y parameter. We use their AGN 8.0 model in this analysis.

To introduce tSZ into our simulations, we extract tSZ cutouts measuring 256 arcmin on a side from the Le Brun et al. (2014) Compton y maps at the locations of massive haloes. We restrict the cutouts to those haloes with $1.75 \times 10^{14}\,M_\odot < M < 3.25 \times 10^{14}\,M_\odot$ and $0.24 < z < 0.56$, as these should be well matched to the real clusters.[4] A cluster with mass $M_{200m} \sim 3.25 \times 10^{14}\,M_\odot$ corresponds roughly to a richness of $\lambda \sim 40$ assuming the mass–richness relation of M17. While some clusters with $\lambda \sim 40$ in our sample may have masses larger than $3.25 \times 10^{14}\,M_\odot$ owing to scatter in the mass–richness relation, we expect the constraint to be dominated by clusters below this mass. Comptonization maps are converted to temperature units assuming an observation frequency of 150 GHz. This process yields 135 simulated tSZ cutouts.

The simulated tSZ cutouts are added to simulated temperature maps at the locations of the mock clusters. We perform the κ estimation process on 2700 mock clusters with added mock tSZ signal. For each cluster, the tSZ signal is rotated by a random angle. With the mock tSZ profiles added to the simulations, the application of the beam, transfer function and noise then proceeds as before and the cutouts are processed through the κ estimation pipeline. The results of this analysis are then compared to a set of simulations that are identical in every way (i.e. the same realizations of CMB, noise, and foregrounds) except they do not have the added tSZ component.

Analysing the simulated cutouts with the mock tSZ signal reveals that the recovered mass in the presence of tSZ is biased low relative to the mass in the absence of tSZ by a few percent. This level of bias

---

[4] Halo masses in M_{500c} are converted to M_{200m} assuming that the mass follows an NFW profile and using the mass-concentration relation from Duffy et al. (2008).

is significantly smaller than the statistical errors associated with our κ estimates.

There is some systematic uncertainty in the simulated tSZ profiles resulting from differences between the Le Brun et al. (2014) simulations and real galaxy clusters. Le Brun et al. (2014) showed that their simulations were able to accurately reproduce the relation between integrated Compton parameter and mass for a set of nearby galaxy clusters observed by Planck Collaboration XI (2011) and Planck Collaboration IV (2013). However, there is significant scatter between the different 'sub-grid' physics models considered by Le Brun et al. (2014). To account for this, we repeat the process of introducing the simulated tSZ profiles into the mock data after increasing the amplitude of the simulated tSZ profiles by 30 per cent. With this increased tSZ amplitude, we find that the bias in the recovered mass estimate increases to roughly 11 per cent. Again, this level of bias is smaller than our statistical error bar, but is certainly non-negligible. We emphasize that this bias is one-sided: it acts to reduce the inferred amplitude of the recovered κ estimate.

We have also repeated the above analysis using a more aggressive gradient filter scale of $l_G = 2000$. This choice yields a higher signal to noise reconstruction of the cluster profile in the absence of tSZ. However, in the presence of tSZ (with amplitude fixed to that of the Le Brun et al. 2014 simulations), choosing $l_G = 2000$ results in recovered mass estimates that are biased low by as much as 30 per cent. Our fiducial choice of l_G therefore has the effect of significantly reducing the bias due to tSZ at the cost of increasing our error bars somewhat.

As a further test of tSZ contamination, we also consider the effect of varying the maximum richness threshold imposed in our analysis of the redMaPPer clusters. Because the amplitude of the tSZ signal for a cluster of mass M scales roughly as $M^{5/3}$ while the lensing signal is roughly proportional to M, we expect high-richness clusters to be more impacted by tSZ bias. Indeed, we find that very high-richness clusters ($\lambda > 100$) tend to exhibit a preference for low masses. One cluster with richness $\lambda \sim 180$ in particular exhibits a fairly significant preference for negative mass. As a result, if we include all the clusters in the analysis, the preference for $A > 0$ actually decreases slightly. However, when varying the richness threshold between $40 < \lambda \lesssim 50$, the preference for $A > 0$ tends to increase with increasing richness threshold. This suggests that tSZ contamination is fairly minimal for clusters in this richness range.

Another way to constrain the presence of tSZ bias in our analysis is to look at the posterior on α. Because high-richness clusters are expected to have their κ estimates biased low by the presence of tSZ, if such bias were significant in our measurement, we would expect the recovered posterior on α to prefer low values. Fig. 4 shows both the prior and posterior on α. The posterior on α is entirely consistent with the prior, suggesting that α is not being driven low by tSZ bias.

In addition to the tSZ effect, galaxy clusters are also expected to distort the CMB via the kinematic SZ effect (kSZ), caused by inverse Compton scattering of CMB photons with electrons that have large bulk velocities relative to the CMB frame. The kSZ is expected to be significantly smaller than the tSZ in most cases, and like the tSZ it is uncorrelated with the CMB gradient behind the cluster. Furthermore, since the sign of the kSZ signal depends on the direction of the cluster peculiar velocity relative to the line-of-sight direction, its effects should be suppressed in an average across many clusters. Consequently, the impact of kSZ on our analysis is expected to be negligible.

7.3.2 Foreground lensing

Our fiducial analysis assumes that all foreground emission is unlensed by the galaxy clusters. However, as described in Section 4.1, some foreground emission may be sourced from behind the cluster and will therefore be gravitationally lensed by the cluster. To determine the bias introduced into our analysis by the assumption of unlensed foreground, we repeat the analysis of the data assuming instead that all foreground emission originates from the surface of last scattering, and is therefore maximally lensed. In that case, the power spectrum of the foreground emission can be simply added to the CMB power spectrum when computing the quadratic estimator. These two extreme assumptions – no foreground lensing or maximal foreground lensing – bracket the possible levels of foreground lensing, and the difference between the two resultant κ estimates provides an (over)estimate of the systematic error introduced into our analysis by our foreground lensing assumption.

When we repeat the analysis of the data with the alternate foreground lensing assumption, we find that the change to the resultant mass constraints is less than 1 per cent, well below our statistical uncertainty.

7.3.3 Miscentring

Our analysis assumes the best-fitting values for the miscentring parameters from Rykoff et al. (2016): $f_{mis} = 0.22$ and $\ln c_{mis} = -1.13$. However, the Rykoff et al. (2016) constraints on the miscentring parameters carry non-negligible uncertainty. To quantify the impact of this uncertainty on our mass–richness constraints, we repeat our analysis with the miscentring parameters increased an amount equal to the 1σ uncertainties from Rykoff et al. (2016): $\sigma(f_{mis}) = 0.11$ and $\sigma(\ln c_{mis}) = 0.22$.

We find that perturbing f_{mis} and $\ln c_{mis}$ by these uncertainties results in changes to A of 3 per cent and 4 per cent, respectively. Adding these uncertainties in quadrature, we therefore introduce a 5 per cent systematic uncertainty to our mass constraints to account for uncertainty on redMaPPer miscentring. This level of uncertainty is roughly 29 per cent of our statistical uncertainty.

It may be surprising that uncertainty on the miscentring parameters introduces such a large systematic error on our mass constraints. Using cluster-galaxy lensing and a similar miscentring model, M17 found that miscentring introduced less than a 1 per cent error on the normalization of the mass–richness relation. This difference in amplitude can be understood as resulting from the different angular scales that contribute to the two constraints. As seen in Fig. 3, the inner most data points exclude $M = 0$ with high significance, suggesting that most of our constraining power is coming from small angular scales where miscentring can have a large impact. The constraint from M17, on the other hand, receives a large contribution from larger scales at which miscentring is unimportant. Indeed, fig. 11 of M17 shows that most of their signal comes from $R > 1$ Mpc, where the effects of miscentring are essentially negligible.

8 DISCUSSION

8.1 Cluster mass constraint from CMB cluster lensing

We have presented a 8.1σ detection of CMB cluster lensing around redMaPPer clusters. Our analysis relied on CMB temperature maps from the SPT-SZ survey and a sample of optically selected galaxy clusters identified in Y1 DES imaging. By fitting the CMB-κ
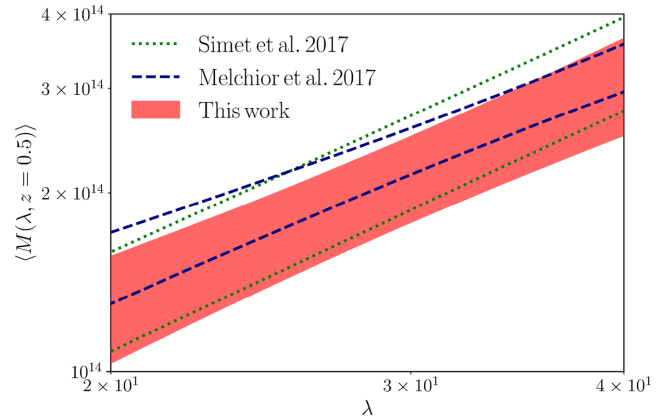
Figure 5. Comparison of constraints obtained on the redMaPPer mass–richness relation from CMB cluster lensing (this work) and cluster-galaxy lensing (Melchior et al. 2017; Simet et al. 2017). The solid band and lines illustrate the 1σ ranges allowed by the different constraints. Note that unlike the Melchior et al. (2017) and Simet et al. (2017) analyses, this work imposes an informative prior on the slope of the mass–richness relation.

measurements around the redMaPPer clusters, we constrained the amplitude of the mass–richness relation to roughly 17 per cent statistical precision.

Our systematics analysis suggests that the dominant systematics affecting our constraints on the redMaPPer mass–richness relation are cluster miscentring and the presence of tSZ. Cluster miscentring contributes a roughly 5 per cent systematic error to our mass constraints. Our analysis attempts to minimize bias due to the tSZ by restricting the cluster sample to $\lambda < 40$ and applying a conservative filter when estimating the CMB temperature gradient field. To estimate residual bias due to the presence of tSZ we analyse simulated data with tSZ profiles taken from the AGN 8.0 simulations of Le Brun et al. (2014) and also employ a data-only consistency test. Both of these tests suggest that there is negligible bias in our analysis due to the tSZ. However, after adjusting the simulations to (conservatively) account for uncertainty in the mock tSZ profiles, we find that the tSZ-caused bias increases to 11 per cent. Note that this bias acts to *reduce* the inferred amplitude of the mass–richness relation, and so should not be thought of as a two-sided uncertainty.

8.2 Comparison to other redMaPPer lensing measurements

The results presented in this work represent the first weak lensing mass calibration of the DES Y1 redMaPPer clusters, and therefore a direct comparison of these results to other weak lensing measurements with the same cluster sample is not yet possible. However, given that the redMaPPer mass–richness relation is expected to be survey-independent to a good approximation, it is possible to compare our results to other recent redMaPPer weak lensing mass constraints.

Fig. 5 compares the constraint obtained here on the cluster mass–richness relation to other constraints obtained from cluster-galaxy lensing. We evaluate all of the various mass–richness relations at $z = 0.5$, the pivot redshift of this analysis and that of M17. The most direct comparison to this work is with the weak lensing mass calibration of DES SV clusters by M17, since that work used the same telescope and similar modelling assumptions. Our constraint on the redMaPPer mass–richness relation is in good agreement with the constraint from M17 over the richness range considered in this work. We prefer a slightly lower normalization of the mass–richness

relation, but this difference is not statistically significant. Note that our analysis uses ∼3700 clusters, while the M17 analysis used only ∼1600 clusters. Our constraint on the mass–richness relation is also in good agreement with recent constraints on the mass–richness relation of redMaPPer clusters in SDSS by S17, shown as the yellow band in Fig. 5. To translate the S17 constraint from the mean redshift of the SDSS sample to $z = 0.5$, we have assumed the redshift scaling and uncertainty from the M17 analysis, i.e. $\beta = 0.18 \pm 0.75$. Were we to instead evaluate the S17 mass–richness relation at the mean redshift of the clusters in that work, the uncertainty on the mass–richness relation would be significantly reduced. Finally, we note that unlike the analyses of M17 and S17, we have imposed an informative prior on α in our analysis (see Table 1). However, as shown in Fig. 4, α is not significantly degenerate with A, given the prior used on α.

8.3 Future prospects

As noted in Section 1, CMB cluster lensing can be used to provide constraints on systematic errors associated with other weak lensing cluster mass constraints. This is possible because the dominant systematics associated with CMB cluster lensing are expected to be essentially uncorrelated with those of galaxy lensing measurements (with miscentring being a notable exception). The weak lensing mass calibration of redMaPPer clusters in M17 obtained a systematic uncertainty of roughly 5 per cent. Their systematic error budget was dominated by photometric redshift uncertainty and shear calibration uncertainty, neither of which affect CMB cluster lensing. Reaching a 5 per cent mass calibration with CMB cluster lensing would require a factor of four improvement in the statistical uncertainties presented here (ignoring, for a moment, the contributions of systematic errors). As we discuss below, such improvements are certainly possible with future data.

One source of systematic uncertainty that is potentially worrying for CMB cluster lensing analyses is the presence of tSZ. Our analysis has shown that if one considers only clusters with masses below about $3.3 \times 10^{14} \, \mathrm{M_\odot}$, the bias introduced into the cluster mass constraints by the tSZ signal – after adopting conservative filtering choices – is at most ∼10 per cent. This is an acceptable level of bias for the analysis presented here given our large statistical error bars. However, with the expected increase in the size of the cluster catalogues from upcoming DES observations, it will be necessary to constrain tSZ biases to better than 10 per cent. There are several possible ways to achieve this goal. First, one can restrict the cluster sample to even lower mass clusters, although this comes at the cost of less signal to noise and reduced cosmological utility. One can also apply more aggressive filtering to remove the tSZ signal, although this will also reduce the signal to noise. Another option is to attempt to model the tSZ signal or apply estimators which are robust to its presence. Finally, one can use the known frequency dependence of the tSZ to construct multifrequency combinations of CMB maps for which the tSZ signal is minimized. It is likely that this last approach will prove essential for future CMB cluster lensing analyses.

Some potential sources of contamination, however, cannot be eliminated with multifrequency information. In particular, the kinematic SZ (kSZ) signal imprinted on the CMB by clusters has the same frequency dependence as the primordial CMB. Because kSZ signal appears as a monopole-like signal on the sky while the lensing signal is dipole-like, it may be possible to effectively fit out the kSZ. Alternatively, one may use polarization information to reconstruct the lensing signal. Because the polarized SZ signals are expected to be much smaller than their temperature-only counterparts,

polarization-sensitive measurements (see below) offer a promising route to obtaining unbiased estimates of the CMB cluster lensing signal (e.g. Raghunathan et al. 2017).

To date, two methods have been applied to measure CMB lensing in the one-halo regime: quadratic estimators (i.e. Madhavacheril et al. 2015; Planck Collaboration XXIV 2016, and this work) and a maximum likelihood approach (i.e. B15). While the maximum likelihood approach in principle offers higher signal to noise, the quadratic estimator has the advantage that it is quite robust to sources of contamination (such as tSZ) in the CMB temperature maps.[5] Indeed, the quadratic estimator approach was employed here because it enabled the use of the 150 GHz SPT-SZ maps despite the fact that these maps also have significant tSZ signal. The 150 GHz maps have significantly higher signal to noise than the tSZ-free linear combination of 90, 150, and 220 GHz maps generated for the maximum likelihood analysis of B15. Furthermore, as shown in Raghunathan et al. (2017), the increased statistical power of the maximum likelihood estimator relative to the quadratic estimator is small for SPT-SZ noise levels.

The reduced noise levels of future CMB experiments, however, make the maximum likelihood estimator approach worth pursuing. If low-noise levels can be achieved in tSZ-cleaned maps then maximum likelihood cluster mass estimation may prove more powerful than the quadratic estimator-based approach. It may also be possible to modify the maximum likelihood technique to increase its robustness to various contaminants by e.g. applying additional filtering to the maps before the estimator is applied.

The future of CMB cluster lensing with DES and SPT is exciting. For the Y1 cluster sample considered here, CMB cluster lensing is useful primarily as a consistency check on the galaxy-lensing-inferred cluster masses. However, five-year DES observations will cover more area and be significantly deeper than DES Y1 observations, resulting in significantly expanded cluster samples, especially at high redshifts. As pointed out in Section 1, it is at high redshifts that CMB cluster lensing has the potential to be competitive with galaxy lensing. Furthermore, new low-noise CMB experiments like SPT-3G (Benson et al. 2014), Advanced ACTpol (Henderson et al. 2016), Simons Array (Suzuki et al. 2016), Simons Observatory, and CMB-S4 (Abazajian et al. 2016) are coming online soon that will significantly improve the signal to noise of CMB cluster lensing measurements (e.g. Louis & Alonso 2017; Raghunathan et al. 2017). These new experiments will also provide low-noise measurements of the CMB polarization signal, which as discussed above, will be useful for constraining biases introduced by the SZ effect.

---

[5] Note that this is not a fundamental limitation of maximum likelihood lensing mass estimation. In principle, one could modify the maximum likelihood estimator to improve its robustness to sources of contamination. However, the simple form of the maximum likelihood estimator considered in B15 was found to be quite sensitive to various contaminants.

REFERENCES

Abazajian K. N. et al., 2016, preprint (arXiv:1610.02743)
Ahn C. P. et al., 2014, ApJS, 211, 17
Applegate D. E. et al., 2014, MNRAS, 439, 48
Bartelmann M., 1996, A&A, 313, 697
Baxter E. J. et al., 2015, ApJ, 806, 247 (B15)
Baxter E. J., Rozo E., Jain B., Rykoff E., Wechsler R. H., 2016, MNRAS, 463, 205
Benson B. A. et al., 2014, in Holland W. S., Zmuidzinas J., eds, Proc. SPIE, Vol. 9153, Millimeter, Submillimeter, and Far-Infrared Detectors and Instrumentation for Astronomy VII. SPIE, Bellingham, p. 91531P
Béthermin M., Wang L., Doré O., Lagache G., Sargent M., Daddi E., Cousin M., Aussel H., 2013, A&A, 557, A66
Birkinshaw M., 1999, Phys. Rep., 310, 97
Carlstrom J. E. et al., 2011, PASP, 123, 568
Crawford T. M. et al., 2014, ApJ, 784, 143
Dawson K. S. et al., 2013, AJ, 145, 10
de Haan T. et al., 2016, ApJ, 832, 95
Diehl H. T. et al., 2014, in Peck A. B., Benn C. R., Seaman R. L., eds, Proc. SPIE, Vol. 9149, Observatory Operations: Strategies, Processes, and Systems V. SPIE, Bellingham, p. 91490V
Diemer B., Kravtsov A. V., 2015, ApJ, 799, 108
Dodelson S., 2004, Phys. Rev. D, 70, 023009
Drlica-Wagner A. et al., 2017, ApJS, preprint (arXiv:1708.01531)
Duffy A. R., Schaye J., Kay S. T., Dalla Vecchia C., 2008, MNRAS, 390, L64
Eisenstein D. J. et al., 2011, AJ, 142, 72
Flaugher B. et al., 2015, AJ, 150, 150
Geach J. E., Peacock J. A., 2017, Nat. Astron., 1, 795
George E. M. et al., 2015, ApJ, 799, 177 (G15)
Henderson S. W. et al., 2016, J. Low Temp. Phys., 184, 772
Hoekstra H., 2001, A&A, 370, 743
Hoekstra H., Bartelmann M., Dahle H., Israel H., Limousin M., Meneghetti M., 2013, Space Sci. Rev., 177, 75
Holder G., Kosowsky A., 2004, ApJ, 616, 8
Hu W., Okamoto T., 2002, ApJ, 574, 566
Hu W., DeDeo S., Vale C., 2007, New J. Phys., 9, 441
Jarvis M. et al., 2016, MNRAS, 460, 2245
Keisler R. et al., 2011, ApJ, 743, 28
Le Brun A. M. C., McCarthy I. G., Schaye J., Ponman T. J., 2014, MNRAS, 441, 1270
Lewis A., King L., 2006, Phys. Rev. D, 73, 063006
Lewis A., Challinor A., Lasenby A., 2000, ApJ, 538, 473
Louis T., Alonso D., 2017, Phys. Rev. D, 95, 043517
Madhavacheril M. et al., 2015, Phys. Rev. Lett., 114, 151302
Mantz A. B. et al., 2015, MNRAS, 446, 2205
Melchior P. et al., 2017, MNRAS, 469, 4899 (M17)
Navarro J. F., Frenk C. S., White S. D. M., 1996, ApJ, 462, 563
Oguri M., Hamana T., 2011, MNRAS, 414, 1851
Planck Collaboration XI, 2011, A&A, 536, A11
Planck Collaboration IV, 2013, A&A, 550, A130
Planck Collaboration XIII, 2016, A&A, 594, A13
Planck Collaboration XXIV, 2016, A&A, 594, A24
Raghunathan S. et al., 2017, J. Cosmol. Astropart. Phys., 8, 030
Rozo E., Rykoff E. S., 2014, ApJ, 783, 80
Rozo E. et al., 2010, ApJ, 708, 645

Rykoff E. S. et al., 2014, ApJ, 785, 104
Rykoff E. S. et al., 2016, ApJS, 224, 1
Schaffer K. K. et al., 2011, ApJ, 743, 90
Schaye J. et al., 2010, MNRAS, 402, 1536
Seljak U., Zaldarriaga M., 2000, ApJ, 538, 57
Shaw L. D., Nagai D., Bhattacharya S., Lau E. T., 2010, ApJ, 725, 1452
Simet M., McClintock T., Mandelbaum R., Rozo E., Rykoff E., Sheldon E., Wechsler R. H., 2017, MNRAS, 466, 3103 (S17)
Story K. T. et al., 2013, ApJ, 779, 86
Suzuki A. et al., 2016, J. Low Temp. Phys., 184, 805
Tinker J. L., Robertson B. E., Kravtsov A. V., Klypin A., Warren M. S., Yepes G., Gottlöber S., 2010, ApJ, 724, 878
Vale C., Amblard A., White M., 2004, New Astron., 10, 1
van Engelen A., Bhattacharya S., Sehgal N., Holder G. P., Zahn O., Nagai D., 2014, ApJ, 786, 13
Yang X., Mo H. J., van den Bosch F. C., Jing Y. P., Weinmann S. M., Meneghetti M., 2006, MNRAS, 373, 1159

[1]*Department of Physics and Astronomy, University of Pennsylvania, Philadelphia, PA 19104, USA*
[2]*School of Physics, University of Melbourne, Parkville, VIC 3010, Australia*
[3]*Kavli Institute for Cosmological Physics, University of Chicago, Chicago, IL 60637, USA*
[4]*Department of Astronomy and Astrophysics, University of Chicago, Chicago, IL 60637, USA*
[5]*Institute of Space Sciences, IEEC-CSIC, Campus UAB, Carrer de Can Magrans, s/n, E-08193 Barcelona, Spain*
[6]*Canadian Institute for Advanced Research, CIFAR Program on Gravity and the Extreme Universe, Toronto, ON M5G 1Z8, Canada*
[7]*Astronomy Department, University of Illinois at Urbana Champaign, 1002 W. Green Street, Urbana, IL 61801, USA*
[8]*Department of Physics, University of Illinois Urbana Champaign, 1110 W. Green Street, Urbana, IL 61801, USA*
[9]*Department of Physics, McGill University, 3600 rue University, Montreal, QC H3A 2T8, Canada*
[10]*Department of Physics, University of Arizona, Tucson, AZ 85721, USA*
[11]*Cerro Tololo Inter-American Observatory, National Optical Astronomy Observatory, Casilla 603, La Serena, Chile*
[12]*Fermi National Accelerator Laboratory, P. O. Box 500, Batavia, IL 60510, USA*
[13]*Department of Physics, University of California, Davis, CA 95616, USA*
[14]*CNRS, UMR 7095, Institut d'Astrophysique de Paris, F-75014 Paris, France*
[15]*Department of Physics and Astronomy, University College London, Gower Street, London WC1E 6BT, UK*
[16]*Sorbonne Universités, UPMC Univ Paris 06, UMR 7095, Institut d'Astrophysique de Paris, F-75014 Paris, France*
[17]*Department of Physics, University of Chicago, 5640 South Ellis Avenue, Chicago, IL 60637, USA*
[18]*Argonne National Laboratory, 9700 South Cass Avenue, Lemont, IL 60439, USA*
[19]*Kavli Institute for Particle Astrophysics and Cosmology, Stanford University, 452 Lomita Mall, Stanford, CA 94305, USA*
[20]*SLAC National Accelerator Laboratory, Menlo Park, CA 94025, USA*
[21]*Enrico Fermi Institute, University of Chicago, Chicago, IL 60637, USA*
[22]*Laboratório Interinstitucional de e-Astronomia – LIneA, Rua Gal. José Cristino 77, Rio de Janeiro, RJ 20921-400, Brazil*
[23]*Observatório Nacional, Rua Gal. José Cristino 77, Rio de Janeiro, RJ 20921-400, Brazil*
[24]*National Center for Supercomputing Applications, 1205 West Clark St, Urbana, IL 61801, USA*
[25]*Institut de Física d'Altes Energies (IFAE), The Barcelona Institute of Science and Technology, Campus UAB, E-08193 Bellaterra (Barcelona), Spain*
[26]*Division of Physics, Mathematics and Astronomy, California Institute of Technology, Pasadena, CA 91125, USA*
[27]*Department of Physics, University of California, Berkeley, CA 94720, USA*
[28]*Department of Physics, IIT Hyderabad, Kandi, Telangana 502285, India*
[29]*Faculty of Physics, Ludwig-Maximilians-Universität, Scheinerstr 1, D-81679 Munich, Germany*
[30]*Excellence Cluster Universe, Boltzmannstr 2, D-85748 Garching, Germany*
[31]*Center for Astrophysics and Space Astronomy, Department of Astrophysical and Planetary Sciences, University of Colorado, Boulder, CO 80309, USA*
[32]*Instituto de Fisica Teorica UAM/CSIC, Universidad Autonoma de Madrid, E-28049 Madrid, Spain*
[33]*European Southern Observatory, Karl-Schwarzschild Straße 2, D-85748 Garching, Germany*
[34]*Institute of Astronomy, University of Cambridge, Madingley Road, Cambridge CB3 0HA, UK*
[35]*Kavli Institute for Cosmology, University of Cambridge, Madingley Road, Cambridge CB3 0HA, UK*
[36]*Universitäts-Sternwarte, Fakultät für Physik, Ludwig-Maximilians Universität München, Scheinerstr 1, D-81679 München, Germany*
[37]*Department of Physics, University of Colorado, Boulder, CO 80309, USA*
[38]*Department of Physics, ETH Zurich, Wolfgang-Pauli-Strasse 16, CH-8093 Zurich, Switzerland*
[39]*Center for Cosmology and Astro-Particle Physics, The Ohio State University, Columbus, OH 43210, USA*
[40]*Department of Physics, The Ohio State University, Columbus, OH 43210, USA*
[41]*University of Chicago, Chicago, IL 60637, USA*
[42]*Astronomy Department, University of Washington, Box 351580, Seattle, WA 98195, USA*
[43]*Astronomy and Astrophysics Department, Santa Cruz Institute for Particle Physics, Santa Cruz, CA 95064, USA*
[44]*Australian Astronomical Observatory, North Ryde, NSW 2113, Australia*
[45]*Physics Division, Lawrence Berkeley National Laboratory, Berkeley, CA 94720, USA*
[46]*Departamento de Física Matemática, Instituto de Física, Universidade de São Paulo, CP 66318, 05314-970 São Paulo, SP, Brazil*
[47]*Steward Observatory, University of Arizona, 933 North Cherry Avenue, Tucson, AZ 85721, USA*
[48]*Department of Physics and Astronomy, George P. and Cynthia Woods Mitchell Institute for Fundamental Physics and Astronomy, Texas A&M University, College Station, TX 77843, USA*
[49]*Department of Astronomy, The Ohio State University, Columbus, OH 43210, USA*
[50]*Department of Physics, University of Michigan, Ann Arbor, MI 48109, USA*
[51]*Department of Astrophysical Sciences, Princeton University, Peyton Hall, Princeton, NJ 08544, USA*
[52]*Department of Astronomy, University of Michigan, Ann Arbor, MI 48109, USA*
[53]*Institució Catalana de Recerca i Estudis Avançats, E-08010 Barcelona, Spain*
[54]*Max Planck Institute for Extraterrestrial Physics, Giessenbachstrasse, D-85748 Garching, Germany*
[55]*Dunlap Institute for Astronomy & Astrophysics, University of Toronto, 50 St George St, Toronto, ON M5S 3H4, Canada*
[56]*Jet Propulsion Laboratory, California Institute of Technology, 4800 Oak Grove Dr., Pasadena, CA 91109, USA*
[57]*Department of Physics, University of Minnesota, Minneapolis, MN 55455, USA*
[58]*Center for Astrophysics and Space Astronomy, Department of Astrophysical and Planetary Sciences, University of Colorado, Boulder, CO 80309, USA*
[59]*NASA Ames Research Center, Moffett Field, CA 94035, USA*
[60]*Department of Physics and Astronomy, University of Sussex, Pevensey Building, Brighton BN1 9QH, UK*
[61]*Physics Department, Center for Education and Research in Cosmology and Astrophysics, Case Western Reserve University, Cleveland, OH 44106, USA*

^{62}*Centro de Investigaciones Energéticas, Medioambientales y Tecnológicas (CIEMAT), Av. Complutense, 40, E-28040 Madrid, Spain*

^{63}*School of Physics and Astronomy, University of Southampton, Southampton SO17 1BJ, UK*

^{64}*Instituto de Física Gleb Wataghin, Universidade Estadual de Campinas, 13083-859 Campinas, SP, Brazil*

^{65}*Jet Propulsion Laboratory, California Institute of Technology, Pasadena, CA 91109, USA*

^{66}*Harvard Smithsonian Center for Astrophysics, 60 Garden St, MS 12, Cambridge, MA 02138, USA*

^{67}*Department of Physics, Stanford University, 382 Via Pueblo Mall, Stanford, CA 94305, USA*

^{68}*Computer Science and Mathematics Division, Oak Ridge National Laboratory, Oak Ridge, TN 37831, USA*

^{69}*Institute of Cosmology and Gravitation, University of Portsmouth, Portsmouth PO1 3FX, UK*

^{70}*Department of Astronomy and Astrophysics, University of Toronto, 50 St George St, Toronto, ON M5S 3H4, Canada*

^{71}*Institute for Astronomy, University of Edinburgh, Edinburgh EH9 3HJ, UK*

This paper has been typeset from a TEX/LATEX file prepared by the author.